Research Square

Preprints are preliminary reports that have not undergone peer review.
They should not be considered conclusive, used to inform clinical practice,
or referenced by the media as validated information.

# Between marine and continental air: atmospheric $CO_2$ variability and local wind associations in coastal Taizhou, China

**Qiao Lu**
Taizhou Meteorological Bureau of Zhejiang Province
**Honghui Xu**
forsnow@126.com
Zhejiang Institute of Meteorological Sciences and National Field Observation and Research Station for Atmospheric Composition Background at Lin'an
**Ziqi Zhang**
Luqiao District Meteorological Bureau of Taizhou
**Meng Shan**
Zhejiang Institute of Meteorological Sciences and National Field Observation and Research Station for Atmospheric Composition Background at Lin'an
**Weidong Dai**
Taizhou Meteorological Bureau of Zhejiang Province
**Wenzhi Zhang**
Taizhou Meteorological Bureau of Zhejiang Province
**Zhimei Weng**
Taizhou Meteorological Bureau of Zhejiang Province
**Kai Wang**
Taizhou Meteorological Bureau of Zhejiang Province

**Research Article**

**Keywords:** Coastal monitoring, Marine air masses, Boundary layer mixing, Atmospheric transport, Potential source regions, Terrestrial ecosystem exchange

**Posted Date:** November 6th, 2026

**DOI:** https://doi.org/10.21203/rs.3.rs-11366198/v1

**License:** This work is licensed under a Creative Commons Attribution 4.0 International License.
Read Full License

**Additional Declarations:** No competing interests reported.

# Between marine and continental air: atmospheric $CO_2$ variability and local wind associations in coastal Taizhou, China

Qiao Lu[1,2], Honghui Xu[3,4]*, Ziqi Zhang[5], Meng Shan[3], Weidong Dai[1], Wenzhi Zhang[1], Zhimei Weng[1,2], Kai Wang[1,2]

[1] Taizhou Meteorological Bureau of Zhejiang Province, Taizhou 318000, China

[2] Taizhou Key Laboratory of Typhoon and Marine Meteorology, Taizhou 318000, China

[3] Zhejiang Institute of Meteorological Sciences and National Field Observation and Research Station for Atmospheric Composition Background at Lin'an, Zhejiang, Hangzhou 311300, China

[4] Zhejiang Provincial Key Laboratory for Research on Industrial Carbon Metrology Technology, Hangzhou 310018, China

[5] Luqiao District Meteorological Bureau of Taizhou, Taizhou 318000, China

* Corresponding author: Honghui Xu. Email: forsnow@126.com

## Abstract

Atmospheric carbon dioxide ($CO_2$) observations at Hongjia, Taizhou, from April 2023 to November 2024 were analyzed using statistical methods, backward-trajectory clustering, the weighted potential source contribution function, and cross-tabulation of trajectory over-ocean fractions and local winds. The mean mole fraction was (440.61 ± 14.0) × $10^{-6}$, lower than at the inland Lin'an station. Concentrations were higher in winter and spring, lower in summer and autumn, and highest around dawn and lowest in the afternoon. Wind speed was negatively correlated with $CO_2$ in all seasons; W–WSW winds were associated with higher concentrations. The 72 h trajectories were classified as continental (over-ocean fraction $f \leq 0.2$), mixed ($0.2 < f < 0.8$), or marine ($f \geq 0.8$). The over-ocean fraction was negatively correlated with $CO_2$ ($r = -0.367$). Marine pathways combined with SE–S winds and speeds ≥ 3 m $s^{-1}$ yielded a mean of 425.8 × $10^{-6}$, whereas continental-pathway means ranged from 448.1 to 449.2 × $10^{-6}$ under different wind filters. Weak westerlies across pathways corresponded to 451.5 × $10^{-6}$, increasing to 459.3 × $10^{-6}$ in winter. Within pathway classes, weak-westerly means exceeded those under other valid wind conditions by 6.9–12.8 × $10^{-6}$. These contrasts cannot independently quantify local anthropogenic contributions. Potential source regions included the Zhejiang–Fujian coast, the Jiangsu–Anhui border, and North China. The findings characterize coastal $CO_2$ variability associated with regional transport, local transport and dispersion, and terrestrial ecosystem exchange.

**Keywords** Coastal monitoring; Marine air masses; Boundary layer mixing; Atmospheric transport; Potential source regions; Terrestrial ecosystem exchange

## Introduction

Carbon dioxide ($CO_2$) is the most important long-lived greenhouse gas affecting the Earth's radiative balance and accounts for approximately 66% of the radiative forcing from long-lived greenhouse gases (World Meteorological Organization [WMO], 2024). Since industrialization, fossil fuel combustion and land-use change have continuously released $CO_2$ into the atmosphere. The global atmospheric mole fraction has risen from approximately $278 \times 10^{-6}$ before industrialization to more than $420 \times 10^{-6}$ in 2023 and continues to increase rapidly (Friedlingstein et al., 2023; WMO, 2024). Oceanic and terrestrial ecosystems together absorb approximately half of anthropogenic $CO_2$ emissions and therefore play a critical role in moderating atmospheric $CO_2$ growth (Ballantyne et al., 2012; Friedlingstein et al., 2023). The Sixth Assessment Report of the Intergovernmental Panel on Climate Change (IPCC, 2021) documents widespread and rapid changes in the climate system and identifies human activities as the principal cause of warming since the mid-twentieth century. Accurate characterization of regional atmospheric $CO_2$ levels, temporal variability, and source–sink processes is consequently important for understanding regional carbon cycling and assessing progress toward carbon peaking and carbon neutrality (Nisbet & Weiss, 2010; Peters et al., 2007).

Ground-based observations and studies of atmospheric $CO_2$ variability have been undertaken in a wide range of regions. The World Meteorological Organization's Global Atmosphere Watch (WMO/GAW) program provides a network of global, regional, and contributing stations for greenhouse gas monitoring (WMO, 2024). China has continued to expand its greenhouse gas observing networks in support of carbon peaking and carbon neutrality, including carbon monitoring and assessment pilot projects operated by the Ministry of Ecology and Environment and the background monitoring network of the China Meteorological Administration. Waliguan in Qinghai and the regional background stations at Shangdianzi in Beijing, Lin'an in Zhejiang, and Longfengshan in Heilongjiang are included in WMO/GAW (Fang et al., 2014). Their observations have been widely used to investigate greenhouse gas levels, variability, trends, and source–sink characteristics (Cheng et al., 2017, 2018; Fang et al., 2015; Fu et al., 2026; Liu et al., 2018; Wei et al., 2020). However, continuous $CO_2$ observations in China have mainly been conducted at inland or urban sites. Long-term continuous observations remain relatively limited

along the coast, particularly at the land–sea interface, and coastal $CO_2$ variability under the combined influence of marine air, terrestrial processes, and human activities is insufficiently characterized.

Coastal observations have particular value for understanding atmospheric $CO_2$ and its sources and sinks. First, coastal areas connect marine and terrestrial environments, where relatively clean marine air, long-range continental transport, and local anthropogenic emissions jointly influence $CO_2$ concentrations. This combination produces complex variability and offers opportunities to investigate regional carbon cycling and air–sea exchange (Chen et al., 2013; Derwent et al., 2002). Second, air arriving from marine sectors can provide observations closer to background conditions and help constrain anthropogenic enhancements relative to the marine background (Brunke et al., 2004; Fang et al., 2015). Third, coastal seas are active regions of biogeochemical cycling and air–sea $CO_2$ exchange; observations contribute to understanding the ocean's role in regulating atmospheric $CO_2$ (Chen et al., 2013; Wanninkhof et al., 2013). Fourth, continuous coastal observations complement the spatial representativeness of inland networks and provide information for regional source–sink assessment, emission inventory evaluation, and mitigation monitoring (Lauvaux et al., 2016; Nisbet & Weiss, 2010). Continuous monitoring and analysis across temporal and spatial scales along the southern coast of the Yangtze River Delta are therefore relevant to both carbon-cycle research and regional monitoring.

Taizhou is located on the central coast of Zhejiang Province and has a coastline of approximately 740 km and extensive adjacent marine areas. It is a representative land–sea interaction region in the southern Yangtze River Delta. $CO_2$ observation stations were established on Dachen Island and at Hongjia in 2022–2023, providing a basis for investigating coastal background conditions and marine and terrestrial influences. Because repeated equipment failures and repairs at Dachen Island caused extended data gaps, this study focuses on continuous $CO_2$ observations and collocated hourly surface meteorological measurements at Hongjia. We characterize temporal $CO_2$ variability, examine associations with wind, temperature, humidity, and pressure, and combine backward-trajectory clustering, the weighted potential source contribution function, and successive filtering by trajectory over-ocean fraction and local wind. The analysis describes characteristic concentration levels associated with marine influence, continental transport, and accumulation under local weak-wind conditions at regional and local scales. The results provide information for understanding coastal $CO_2$ variability, improving the coastal coverage of China's greenhouse gas observing network, and supporting regional carbon monitoring and assessment.

## Materials and methods

### Observation site

The Hongjia greenhouse gas observation station (121°25′ E, 28°39′ N) is located on the rooftop of the Meteorological Disaster Prevention and Mitigation Center in Hongjia Subdistrict, Jiaojiang District, Taizhou. The greenhouse gas analyzer is housed in an enclosure beneath the observation tower, with real-time data transmission. The $CO_2$/$CH_4$ sampling inlet is mounted on a steel tower 15 m above ground level. The station lies in the southern Yangtze River Delta close to the East China Sea. Residential areas and a small number of industrial facilities are located to the east, with an industrial park approximately 3 km from the station. The area within 10 km to the south is predominantly residential. Roads, industrial facilities, and residential areas are more abundant to the west and north; the principal nearby industrial areas are within 1 km to the west and 3 km to the north.

### Measurement instrument

Atmospheric greenhouse gases at Hongjia were measured using an LGR high-precision greenhouse gas analyzer (GLA331-GGA, ABB), based on off-axis integrated cavity output spectroscopy (OA-ICOS). The instrument uses the cavity-enhanced absorption technology developed by Los Gatos Research to measure $CH_4$, $CO_2$, and $H_2O$ simultaneously and continuously. OA-ICOS provides an extended optical path for sensitive gas measurements while reducing the dependence on precise optical alignment (Baer et al., 2002). The analyzer has a wide measurement range, high precision, low drift, and low cross-interference. Its optical configuration is simpler than that used in conventional cavity ring-down spectroscopy, supporting stable operation with low zero and span drift. Data recording can begin approximately 20 s after startup. The measurement ranges extend to 100 ppm for $CH_4$ and 20,000 ppm for $CO_2$. The reported 1 s measurement precision is better than 0.6 ppb for $CH_4$ and 0.15 ppm for $CO_2$, and the maximum drift over 24 h is less than 3 ppb and 0.2 ppm, respectively. These performance characteristics support long-term continuous greenhouse gas observations at Hongjia.

### Data processing and trajectory analysis

Abnormal observations were removed using station operation logs to identify instrument failures and other disturbances, including unstable calibration gas, shutdowns for maintenance, blocked

condensation tubing, and nearby combustion events. Valid 5 min averages were then aggregated into hourly mean $CO_2$ concentrations. Concentrations are expressed as mole fractions in units of $\times 10^{-6}$ throughout this paper.

Because $CO_2$ is long-lived, its variability reflects emissions and changing meteorological conditions across multiple scales. To examine regional atmospheric transport, 72 h backward trajectories were calculated using the Hybrid Single-Particle Lagrangian Integrated Trajectory (HYSPLIT) model and global meteorological data from the NOAA Air Resources Laboratory (Draxler & Hess, 1998; Stein et al., 2015). Trajectory clustering was performed using MeteoInfo, with an arrival height of 500 m and angular distance as the clustering criterion (Wang, 2014). One trajectory was calculated every 6 h. Trajectory arrival times, $CO_2$ measurements, and meteorological observations were matched using the same Coordinated Universal Time (UTC). The land–sea status of hourly trajectory endpoints was determined using the Natural Earth 1:10 million global land polygons (Natural Earth, n.d.). The over-ocean fraction was calculated as the number of endpoints over the ocean divided by 73, including the arrival endpoint. This fraction describes the marine versus terrestrial portions of the trajectory pathway.

The potential source contribution function (PSCF) was used to examine the spatial distribution of potential source regions. PSCF represents the conditional probability that an air mass passing through a grid cell arrives at the receptor with a concentration exceeding a specified threshold (Ashbaugh et al., 1985; Lupu & Maenhaut, 2002). It is defined as

$$\mathrm{PSCF}_{ij} = \mathrm{M}_{ij} / \mathrm{N}_{ij} \quad (1)$$

where $N_{ij}$ is the total number of backward-trajectory endpoints in grid cell (i, j), and $M_{ij}$ is the number of endpoints in that cell associated with high $CO_2$ concentrations at arrival. The threshold was the seasonal mean background concentration obtained from a smoothed fit.

To reduce the influence of grid cells with small endpoint counts, a weighting coefficient $W_{ij}$ was applied:

$$\mathrm{WPSCF}_{ij} = \mathrm{W}_{ij} \times \mathrm{PSCF}_{ij} \quad (2)$$

The weighted potential source contribution function (WPSCF) is thus the product of PSCF and $W_{ij}$. The weighting coefficients used in this study were

$$W_{ij} = \begin{cases} 1, & N_{ij} > 4N_{ave} \\ 0.7, & N_{ave} < N_{ij} \leq 4N_{ave} \\ 0.42, & 0.5N_{ave} < N_{ij} \leq N_{ave} \\ 0.05, & N_{ij} \leq 0.5N_{ave} \end{cases} \quad (3)$$

where $N_{ave}$ is the mean number of trajectories passing through grid cells within the study domain. The weighting reduces the influence of poorly sampled cells in the potential source analysis (Lupu & Maenhaut, 2002). The trajectory statistics identify associations between pathways and receptor concentrations; individual trajectories do not fully represent turbulent dispersion (Stohl, 1998).

## Results and discussion

### Seasonal evolution of $CO_2$ concentrations

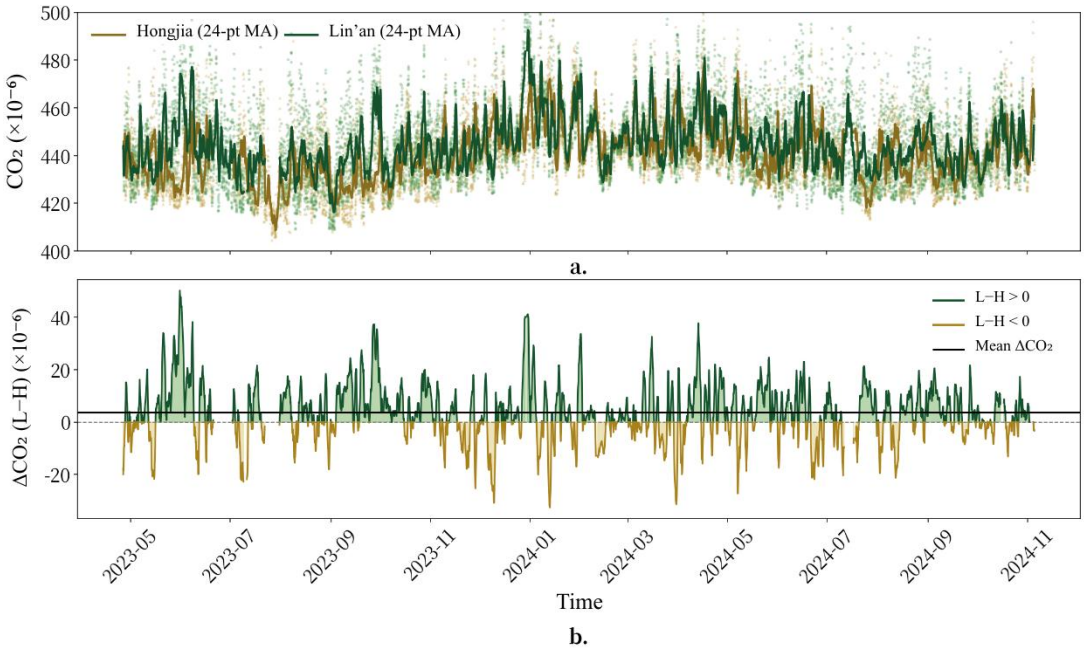


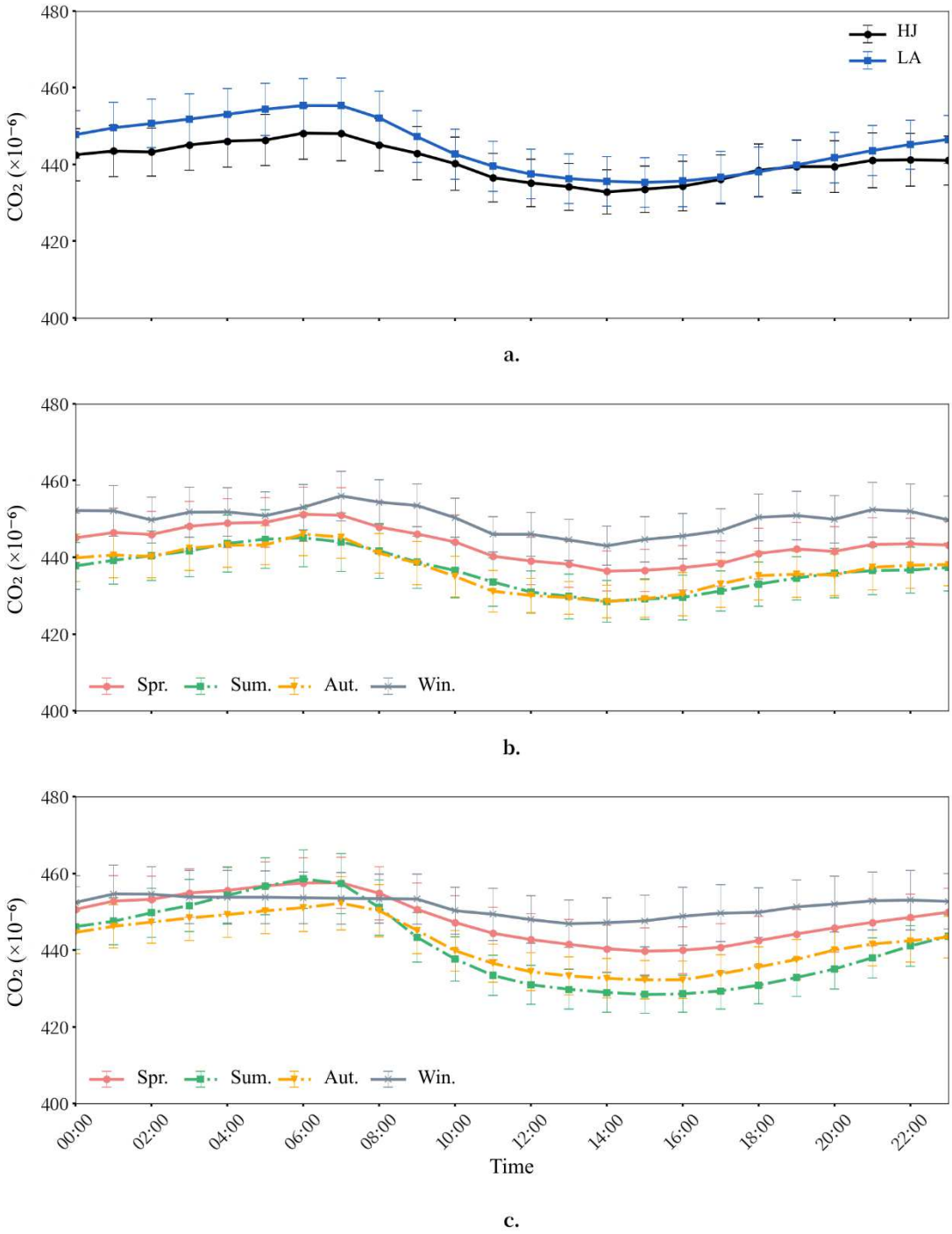

**Fig. 1** $CO_2$ time series at Hongjia and Lin'an during the observation period (a) and the concentration difference between the stations (b). Colored points in (a) represent hourly observations and curves show 24-point moving averages (MA). L−H denotes Lin'an minus Hongjia; the horizontal line in (b) denotes the mean difference

Figure 1a shows the hourly $CO_2$ concentrations at Hongjia and Lin'an from April 2023 to November 2024. Colored points represent hourly observations, and the curves are 24-point moving averages. The mean concentrations over the observation period were (440.61 ± 14.0) × $10^{-6}$ at Hongjia and (444.66 ± 14.9) × $10^{-6}$ at Lin'an. Both stations showed pronounced and

broadly synchronous seasonal variability, with concentrations increasing from September to the following January and declining with fluctuations from February to July. Concentrations were therefore highest in winter and lowest in summer. The maximum and minimum smoothed concentrations at Hongjia were $477.4 \times 10^{-6}$ and $408.7 \times 10^{-6}$, respectively, with the minimum occurring in July. The corresponding values at Lin'an were $492.6 \times 10^{-6}$ and $416.3 \times 10^{-6}$.

The comparison between stations (Fig. 1b) indicates that the mean $CO_2$ concentration at Lin'an was approximately $4 \times 10^{-6}$ higher than at Hongjia. For observations matched by hour, the mean difference (Lin'an minus Hongjia) was $(3.7 \pm 14.8) \times 10^{-6}$, and the correlation between the two series was approximately 0.46. The mean difference was largest in spring and autumn, at approximately $4.8 \times 10^{-6}$, and smallest in winter, at approximately $1.5 \times 10^{-6}$. Although the station means were most similar in winter, hourly differences were more variable during that season. These contrasts are consistent with differences in the surrounding land cover and air-mass origins. Hongjia is a coastal station and is frequently influenced by relatively clean marine air, whereas inland Lin'an is more exposed to regional anthropogenic emissions and terrestrial ecosystem respiration (Cheng et al., 2018; Fang et al., 2014; Liu et al., 2018). Prevailing northerly flow in winter can transport continental air with higher $CO_2$ concentrations toward the coast, increasing concentrations at Hongjia and narrowing the difference between the stations.

186 Diurnal variation of $CO_2$ concentrations




187

188 **Fig. 2** Mean diurnal $CO_2$ cycles at Hongjia and Lin'an over the observation period (a) and seasonal cycles at Hongjia
189 (b) and Lin'an (c). HJ and LA denote Hongjia and Lin'an, respectively; Spr., Sum., Aut., and Win. denote spring,
190 summer, autumn, and winter

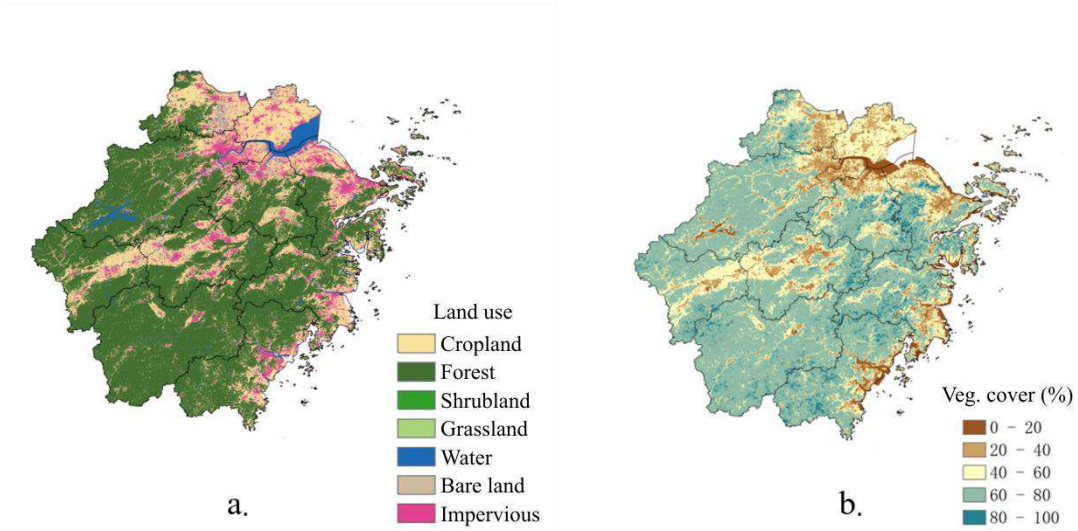



**Fig. 3** Land-use types (a) and vegetation coverage (b) in Zhejiang Province in 2023. Veg. cover denotes vegetation coverage; impervious denotes impervious surfaces

Figure 2 presents the diurnal $CO_2$ cycles at Hongjia and Lin'an. Figure 2a shows the mean cycle over the observation period, and Fig. 2b and c show the seasonal cycles at Hongjia and Lin'an, respectively. Both stations exhibited lower daytime and higher nighttime concentrations, reflecting the combined influence of meteorological conditions and biological activity. Between 07:00 and 14:00, increasing surface temperature and the erosion of the nocturnal inversion promote vertical turbulent mixing (Stull, 1988). The land-use and vegetation maps of Zhejiang Province (Fig. 3) indicate that the area surrounding Hongjia is predominantly cropland, with vegetation coverage of 40–60%. Photosynthetic uptake by cropland vegetation contributes to the daytime decline in $CO_2$, consistent with observations in other cropland areas of the Yangtze River Delta (Duan et al., 2021). The minimum occurred at approximately 14:00, with a concentration of $(431.76 \pm 15.0) \times 10^{-6}$. At night, photosynthetic uptake ceases while respiration continues, and a near-surface radiative inversion favors $CO_2$ accumulation. Concentrations peaked around 07:00 at $(446.04 \pm 16.7) \times 10^{-6}$. Morning and evening periods coincide with commuting peaks, when vehicle emissions may further enhance near-surface $CO_2$ (Pataki et al., 2006; Wei et al., 2020).

The diurnal cycle at Lin'an was broadly in phase with that at Hongjia, with higher concentrations around dawn and lower concentrations in the afternoon. The maximum occurred near 06:00 at $(455.35 \pm 14.1) \times 10^{-6}$, and the minimum near 15:00 at $(435.29 \pm 13.0) \times 10^{-6}$. The afternoon minimum therefore lagged that at Hongjia by approximately 1 h. Concentrations at Lin'an were higher throughout the day, and the diurnal range was larger, at approximately $20 \times 10^{-6}$ compared with approximately $15 \times 10^{-6}$ at Hongjia. Figure 3 shows that Lin'an is located in the

mountainous and hilly terrain of northwestern Zhejiang, where forest is the predominant surrounding land cover and vegetation coverage generally exceeds 60%. The diurnal transition between photosynthetic uptake and respiration in these terrestrial ecosystems can enhance the $CO_2$ cycle (Baldocchi, 2003; Fang et al., 2014). At coastal Hongjia, mixing with relatively clean marine air is consistent with the smaller diurnal amplitude. Vegetation and air-mass origin thus provide plausible explanations for the contrasting diurnal amplitudes.

$CO_2$ exhibited a similar daily cycle with a single afternoon minimum in all seasons. At Hongjia (Fig. 2b), concentrations were generally higher in spring and winter than in summer and autumn. The highest seasonal hourly mean occurred at 07:00 in winter, at $(453.43 \pm 13.3) \times 10^{-6}$, consistent with accumulation under a strong morning inversion combined with anthropogenic emissions. The lowest occurred at 14:00 in autumn, at $(428.42 \pm 8.7) \times 10^{-6}$, when photosynthetic uptake and atmospheric dispersion favor lower concentrations. At Lin'an (Fig. 2c), the diurnal amplitude was largest in summer and smallest in winter, when the cycle was nearly flat. The highest value occurred around 06:00 in summer, at $(458.52 \pm 15.3) \times 10^{-6}$, and the lowest around 15:00 in summer, at $(428.45 \pm 9.7) \times 10^{-6}$. Strong summer photosynthesis and respiration can produce this large day–night contrast, emphasizing the influence of biological exchange in inland forested environments (Baldocchi, 2003; Graven et al., 2013).

Monthly and seasonal distributions of $CO_2$ concentrations

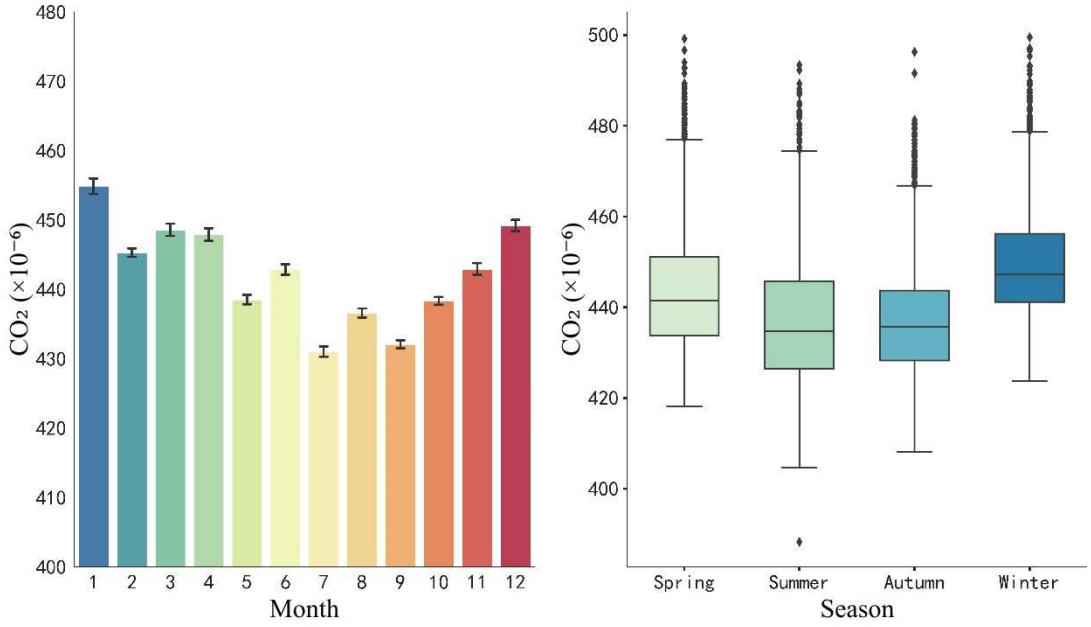



**Fig. 4** Monthly means (a) and seasonal distributions (b) of $CO_2$ at Hongjia. In (b), box edges denote the 25th and 75th percentiles, the central line the median, colored central markers the seasonal mean, and whiskers the 5th and 95th percentiles. Error bars represent standard deviations

The monthly means and seasonal distributions at Hongjia are shown in Fig. 4. The highest monthly mean occurred in January, at (454.93 ± 14.9) × $10^{-6}$, and the lowest in July, at (431.08 ± 12.7) × $10^{-6}$. The difference between the monthly maximum and minimum was approximately 24 × $10^{-6}$. Following the July minimum, concentrations generally increased, with fluctuations, toward the January maximum. September concentrations, at approximately 432 × $10^{-6}$, remained close to the low levels observed in July and August rather than increasing markedly as temperature declined. Continued warmth and active crop growth may sustain photosynthetic uptake during this period, while southerly marine air can maintain relatively clean background conditions. Both processes are consistent with the limited recovery in September (Duan et al., 2021; Wei et al., 2020).

The seasonal mean concentrations were (443.51 ± 13.6) × $10^{-6}$ in spring, (436.68 ± 13.7) × $10^{-6}$ in summer, (436.96 ± 12.1) × $10^{-6}$ in autumn, and (449.89 ± 12.5) × $10^{-6}$ in winter. This distribution indicates higher concentrations in winter and spring and lower concentrations in summer and autumn. Stronger photosynthetic uptake under abundant sunlight and active vegetation growth contributes to the lower summer and autumn concentrations. In spring, vegetation begins to recover, but lower temperatures may limit photosynthetic uptake, resulting in higher concentrations than in summer and autumn. Several processes can contribute to the winter

maximum: reduced photosynthesis during vegetation dormancy, stable stratification and near-surface inversions that suppress vertical dispersion, and winter monsoon transport of continental air with higher $CO_2$ concentrations. Increased fossil fuel and biomass combustion may provide additional anthropogenic inputs (Fu et al., 2026; Liu et al., 2018; Wei et al., 2020). The seasonal cycle at Hongjia therefore reflects the combined influence of source–sink activity, atmospheric dispersion, transport, and human activities, consistent with the broader role of terrestrial exchange in atmospheric $CO_2$ seasonality (Graven et al., 2013).

## Influence of meteorological conditions on $CO_2$ concentrations

### Correlations with meteorological variables

Seasonal correlations were examined between hourly $CO_2$ concentrations and four meteorological variables: temperature, relative humidity, 10 min mean wind speed, and sea-level pressure (Fig. 5). Most correlations passed significance tests because of the large sample size, but their magnitudes were generally weak to moderate, mostly around $|r| = 0.1–0.4$. The results indicate that $CO_2$ variability was associated with multiple meteorological conditions and source–sink processes. Wind speed had the strongest overall association, with negative correlations in all seasons ranging from −0.27 to −0.40 and a mean absolute correlation of approximately 0.33. Temperature and relative humidity had similar mean absolute correlations of approximately 0.22, whereas sea-level pressure showed the weakest overall association.

Temperature was negatively correlated with $CO_2$ in all seasons, most strongly in autumn ($r = −0.44$). This association is consistent with the influence of photosynthesis: increasing daytime temperature can coincide with stronger carbon uptake and lower atmospheric $CO_2$ (Baldocchi, 2003; Duan et al., 2021). In autumn, continued crop growth, substantial temperature variability, and relatively limited anthropogenic and weather-related disturbances may make this relationship clearer. In summer, high temperatures can enhance both respiration and photosynthesis, partly offsetting their effects, while convective mixing adds further variability. In winter, vegetation dormancy weakens the coupling between photosynthesis and temperature, and stratification and regional transport become more influential. Spring represents an intermediate period of vegetation recovery. Separate daytime and nighttime analyses (not shown) indicated a stronger negative correlation during the day, especially in autumn. Daytime warming accompanies photosynthetic uptake, whereas at night photosynthesis ceases and respiration releases $CO_2$.

Although low nighttime temperatures can reduce respiration, near-surface $CO_2$ continues to accumulate, weakening the temperature–$CO_2$ relationship.

Relative humidity was positively correlated with $CO_2$ in all seasons, with r ranging from 0.18 to 0.30. High humidity often coincides with weak winds and stable conditions that inhibit dispersion and favor near-surface accumulation. It can also accompany cloudy or rainy conditions with reduced solar radiation and photosynthetic uptake. These mechanisms are consistent with the positive humidity–$CO_2$ association but do not establish an independent humidity effect (Duan et al., 2021; Wei et al., 2020).

Sea-level pressure showed the weakest overall correlation with $CO_2$. Absolute correlations were below 0.1 in most seasons, with a clearer positive association in autumn ($r = 0.30$). High-pressure conditions in autumn can coincide with subsidence and stable stratification that inhibit boundary layer development and vertical dispersion, favoring near-surface accumulation (Stull, 1988). In the other seasons, pressure was intertwined with temperature and wind conditions and showed no consistent statistical association.

Overall, wind speed and temperature had the clearest associations with $CO_2$ variability, consistent with dispersion and biological uptake, respectively. Relative humidity and sea-level pressure may provide additional information about atmospheric stability and photosynthetic conditions. Seasonal differences in these correlations reflect changes in the relative roles of source–sink activity and atmospheric dispersion.

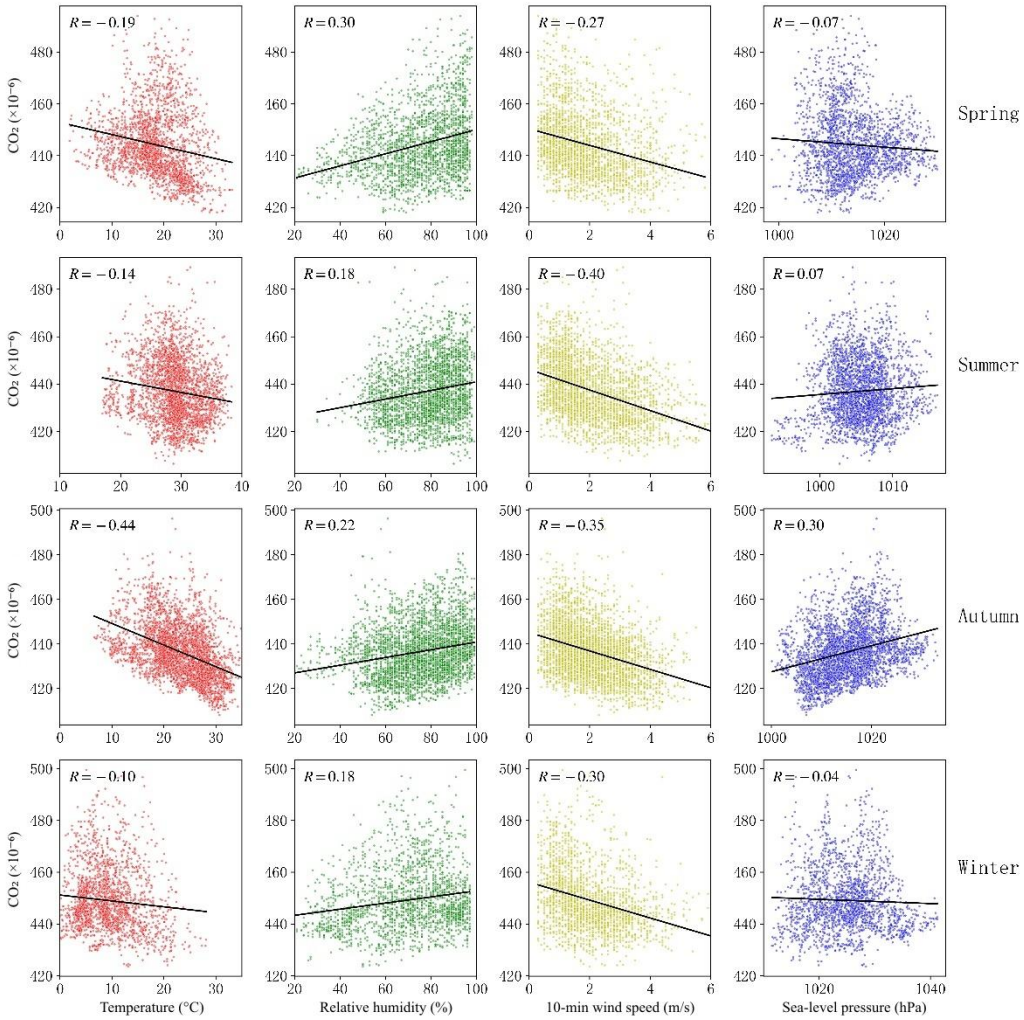



**Fig. 5** Relationships between $CO_2$ concentration and temperature, relative humidity, 10 min mean wind speed, and sea-level pressure at Hongjia in spring, summer, autumn, and winter

## Influence of surface winds

Wind speed and direction are important for the transport, dilution, and dispersion of atmospheric constituents. As shown in Fig. 5, wind speed was negatively correlated with $CO_2$ in every season. Increasing wind speed promotes turbulent dispersion and horizontal transport, whereas weak winds and stable conditions favor near-surface accumulation. Wind direction additionally indicates the spatial distribution of surrounding sources and sinks, because air arriving from different sectors can carry different $CO_2$ loads (Liu et al., 2018; Wei et al., 2020).

The seasonal wind-direction–concentration roses (Fig. 6a–d) show that the highest concentrations occurred under W–WSW winds in all four seasons: approximately $452 \times 10^{-6}$ in spring, $445 \times 10^{-6}$ in summer, $448 \times 10^{-6}$ in autumn, and $457 \times 10^{-6}$ in winter. Mean wind speeds in this sector were relatively low. This sector corresponds to the industrial area within 1 km west of the station.

Nearby emissions, dense buildings, and weak ventilation are consistent with $CO_2$ accumulation from this direction. Westerly enhancements were particularly pronounced in autumn and winter (Fig. 6c and d), whereas concentrations were more evenly distributed across directions in spring and summer. Southerly winds generally corresponded to lower concentrations, consistent with the absence of major industrial sources south of the station and the frequent arrival of relatively clean marine air. In winter, concentrations under E–ENE–NE winds remained relatively high, at approximately $451 \times 10^{-6}$, despite mean wind speeds of 2–2.5 m $s^{-1}$ (Fig. 6d). Transport from the eastern industrial park may contribute to this feature.

The monthly concentration roses are shown in Fig. 7a–l. The wind-direction frequency roses (Fig. 8a–d) indicate a seasonal transition from predominantly easterly winds (E–ENE) in spring to southerly winds (S–SSW) in summer and west-northwesterly to northwesterly winds (WNW–NW) in autumn and winter. Despite this shift in prevailing direction, elevated $CO_2$ concentrations remained associated with the western sector throughout the year (W–WSW–WNW in Fig. 7a–l), consistent with persistent nearby industrial influences. Monthly concentrations were higher in winter and early spring (December–March; Fig. 7a–c and l), declined during April–June as easterly and southerly winds became more frequent (Fig. 7d–f), and reached their minimum in July (Fig. 7g). Low concentrations persisted from summer into early autumn (Fig. 7g–i), followed by an increase after October as northwesterly winds returned (Fig. 7j–l). This cycle reflects the seasonal alternation between frequent marine airflow in summer and continental airflow combined with accumulation near western sources in winter (Cheng et al., 2018; Wei et al., 2020).

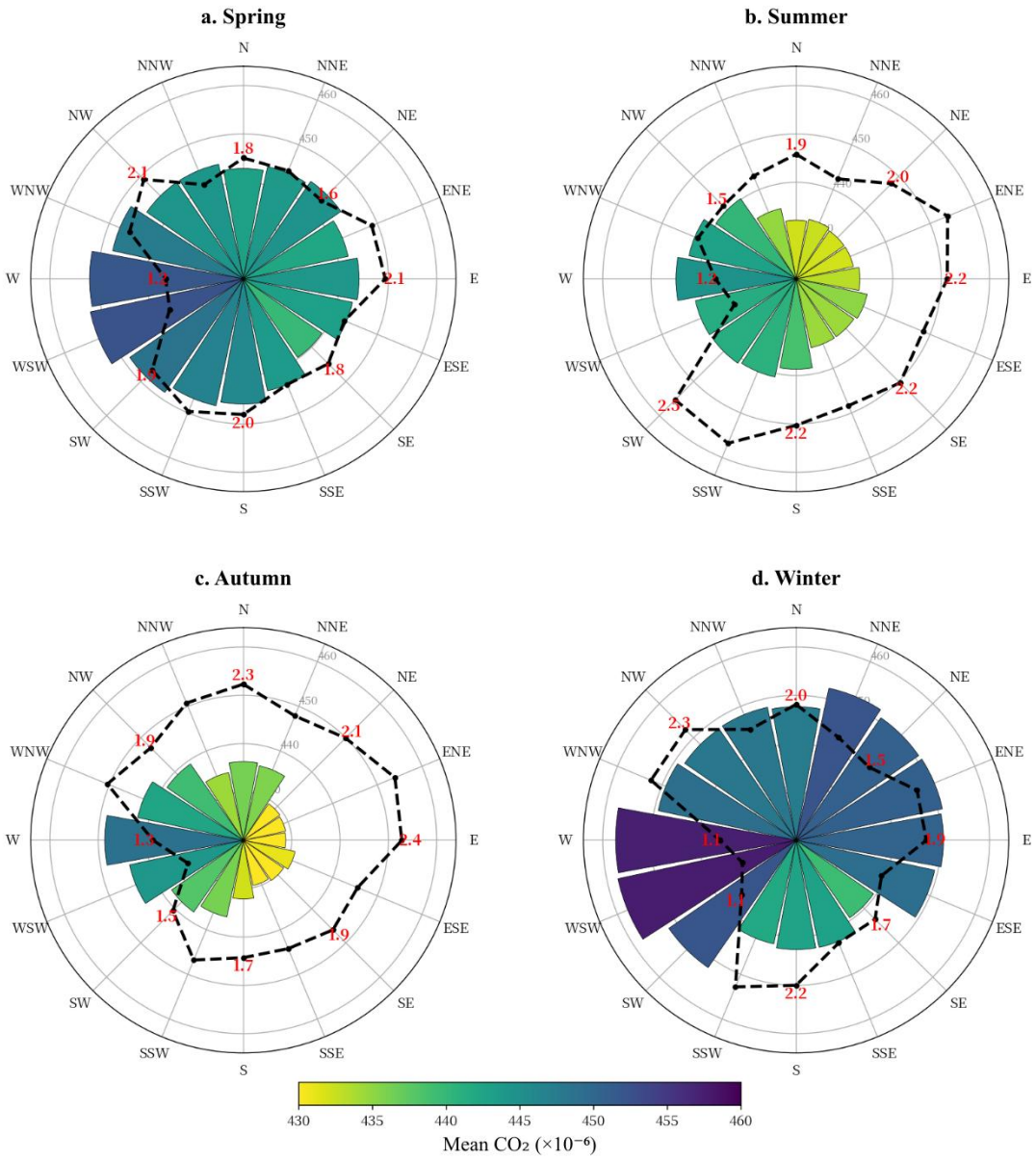
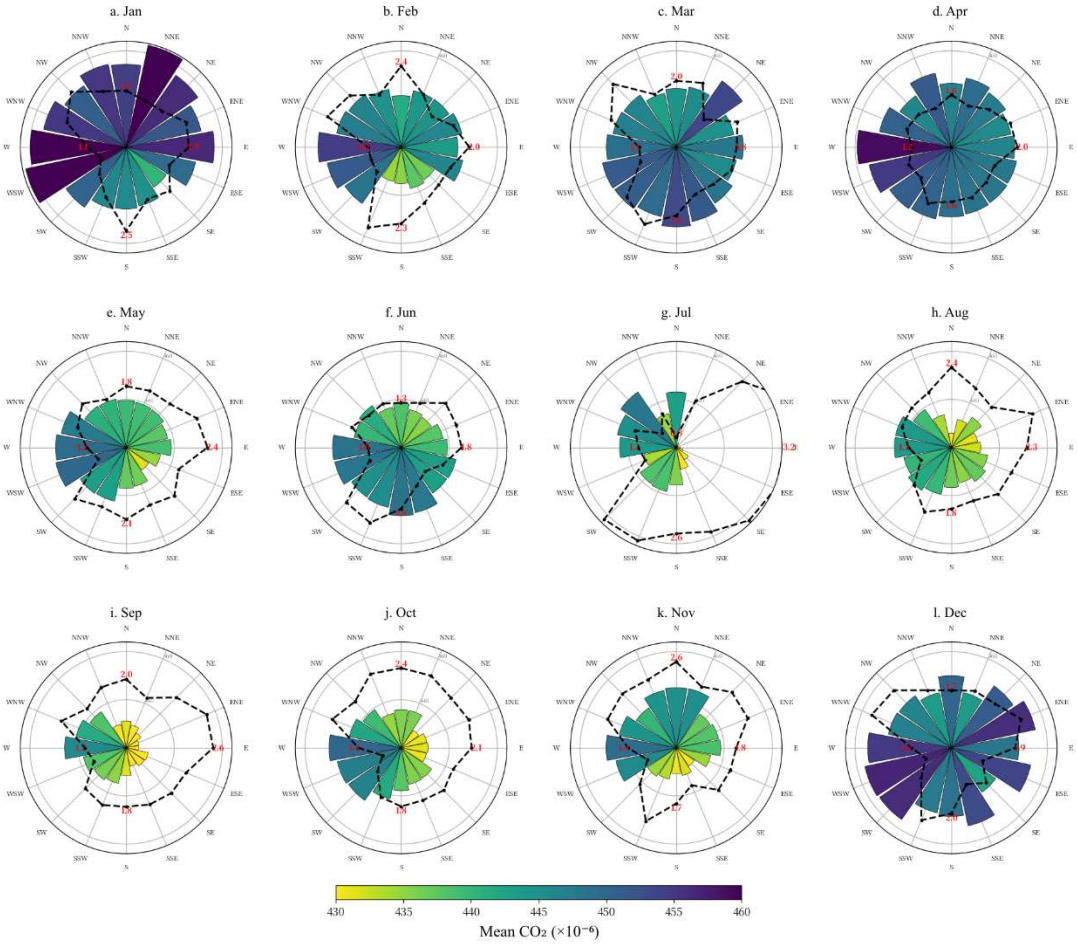



**Fig. 6** Mean $CO_2$ concentration and mean wind speed for the 16 wind directions in each season at Hongjia. Sector-bar length and color indicate mean $CO_2$ concentration; the black dashed curve and red numbers indicate mean wind speed ($m\ s^{-1}$)




341

342 **Fig. 7** Mean $CO_2$ concentration and mean wind speed for the 16 wind directions in each month at Hongjia. The
343 legend is the same as in Fig. 6

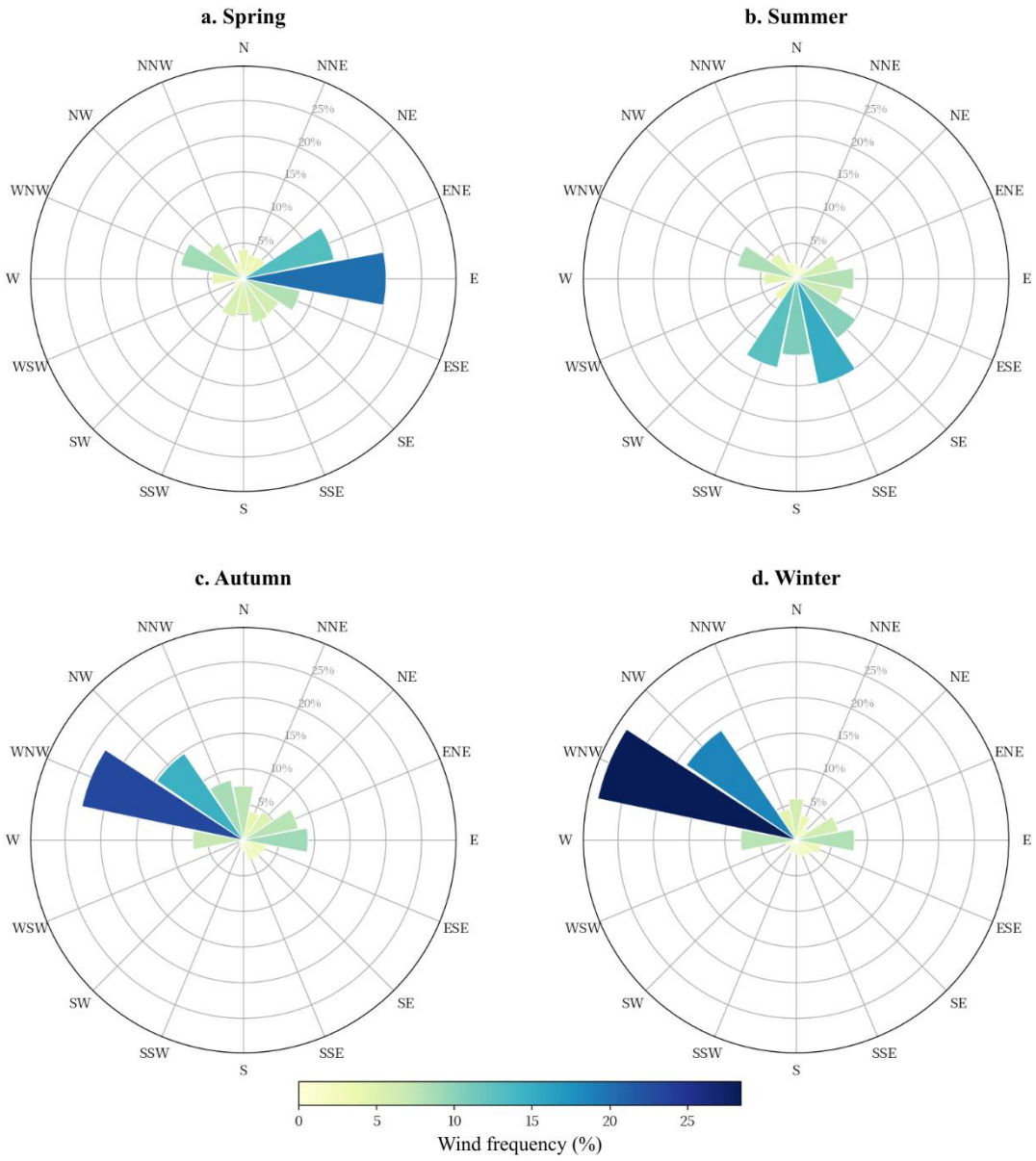



**Fig. 8** Seasonal wind-direction frequency roses at Hongjia. Sector-bar length and color indicate wind-direction frequency (%)

To describe the influence of wind speed, occurrence frequencies and corresponding mean $CO_2$ concentrations were calculated for each wind-force class by season (Table 1). Classes 1–2, representing weak winds of ≤ 3.3 m $s^{-1}$, accounted for approximately 85–89% of observations in each season. Concentrations declined with increasing wind speed across the frequently observed classes. The highest values occurred in class 1: 449.2 × $10^{-6}$ in spring, 443.3 × $10^{-6}$ in summer, 441.6 × $10^{-6}$ in autumn, and 454.4 × $10^{-6}$ in winter. By class 3, the means had declined to 438.9, 429.9, 428.9, and 444.0 × $10^{-6}$, respectively. Winds in class 4 occurred in less than 1% of observations in each season, limiting the interpretation of that group. The overall negative relationship is consistent with accumulation of local and nearby emissions under weak winds and

inhibited dispersion, followed by dilution as ventilation increases. Thus, elevated $CO_2$ concentrations at Hongjia were associated with the combination of weak-wind conditions and transport from nearby western sources. The regional transport analysis below further examines the role of air-mass pathways.

**Table 1** Occurrence frequency and mean $CO_2$ concentration by wind-force class and season

| Statistic | Season | 0.3–1.5 m s⁻¹ Class 1 | 1.6–3.3 m s⁻¹ Class 2 | 3.4–5.4 m s⁻¹ Class 3 | 5.5–7.9 m s⁻¹ Class 4 |
|---|---|---|---|---|---|
| Frequency | Spring | 50.82% | 37.90% | 11.04% | 0.24% |
| | Summer | 44.49% | 40.69% | 13.89% | 0.93% |
| | Autumn | 38.34% | 50.44% | 10.97% | 0.24% |
| | Winter | 45.37% | 44.08% | 10.19% | 0.37% |
| Mean $CO_2$ ($\times 10^{-6}$) | Spring | 449.21 | 441.79 | 438.94 | 443.50 |
| | Summer | 443.31 | 434.80 | 429.91 | 423.42 |
| | Autumn | 441.61 | 435.18 | 428.87 | 438.09 |
| | Winter | 454.39 | 446.65 | 443.98 | 446.78 |

## Influence of regional transport and local winds on $CO_2$ concentrations

### Seasonal clustering of 72 h backward trajectories

Seasonal HYSPLIT trajectory clustering was used to characterize air-mass pathways and their associated $CO_2$ concentrations from April 2023 to November 2024. The four seasons included 2,240 trajectories, of which 2,150 could be matched to valid $CO_2$ observations at arrival. The valid concentration-matched trajectory counts were 510 in spring, 659 in summer, 618 in autumn, and 363 in winter. Within each season, trajectories associated with concentrations at or above the 80th percentile were defined as high-concentration trajectories, and those at or below the 20th percentile as low-concentration trajectories. These categories describe the concentration distributions associated with different pathways.

Figure 9 and Table 2 indicate that, in spring, 36.72% of the trajectories originated from the Hebei–Shanxi region (cluster 1), 23.63% from west of Taiwan (cluster 2), 16.60% from the Jilin–Liaoning border region (cluster 3), and 23.05% from the East China Sea (cluster 4). Cluster 2 moved relatively slowly and had the highest mean $CO_2$ concentration, at $448.0 \times 10^{-6}$. Cluster 1 was the most frequent and had a mean of $445.7 \times 10^{-6}$. Cluster 4 predominantly followed marine

pathways and contained more low-concentration trajectories; its mean was the lowest, at 436.7 × $10^{-6}$.

In summer, 31.11% of the trajectories originated near the Ryukyu Islands in the East China Sea (cluster 1), 56.25% from the South China Sea (cluster 2), and 12.64% from the Yellow Sea south of the Shandong Peninsula (cluster 3). Cluster 1 crossed the open ocean and had the lowest mean $CO_2$ concentration, at 430.4 × $10^{-6}$. Cluster 2 traveled along the Zhejiang–Fujian coast and had a mean of 441.1 × $10^{-6}$, whereas cluster 3 had a mean of 438.4 × $10^{-6}$. Although summer trajectories often crossed marine areas, coastal transport and open-ocean pathways were associated with different concentration levels.

In autumn, 40.45% of the trajectories originated from the Inner Mongolia–Liaoning region (cluster 1), 25.95% from marine areas southeast of Zhejiang (clusters 2 and 5), 24.52% from the Yellow Sea (cluster 3), and 9.08% from central and northern Inner Mongolia (cluster 4). Cluster 4 passed through Shanxi, Henan, and Anhui and had the highest mean concentration, at 444.0 × $10^{-6}$. Cluster 2 had the lowest mean, at 430.6 × $10^{-6}$, while the means for clusters 1, 3, and 5 were 436.9, 435.6, and 435.3 × $10^{-6}$, respectively. In winter, cluster 1 traveled southward from North China and accounted for 60.99% of trajectories, with a mean of 450.2 × $10^{-6}$. Clusters 2 and 3 had means of 449.3 and 447.7 × $10^{-6}$, respectively. Clusters 1 and 2 together accounted for 82.14% of winter trajectories and represented the principal transport pathways.

These results indicate that open-ocean pathways generally corresponded to lower concentrations, while continental and coastal pathways corresponded to higher concentrations. Slowly moving air masses may also be influenced by nearby emissions and limited dispersion, consistent with the transport dependence of $CO_2$ observed at other Chinese stations (Cheng et al., 2017, 2018; Liu et al., 2018). Seasonal trajectory clusters describe pathway geometry and cannot be equated directly with the marine, mixed, and continental categories defined by the over-ocean fraction. Cluster numbers and their associated concentrations are retained here, whereas individual trajectories are assigned to land–sea pathway categories using the common over-ocean fraction criteria described below.

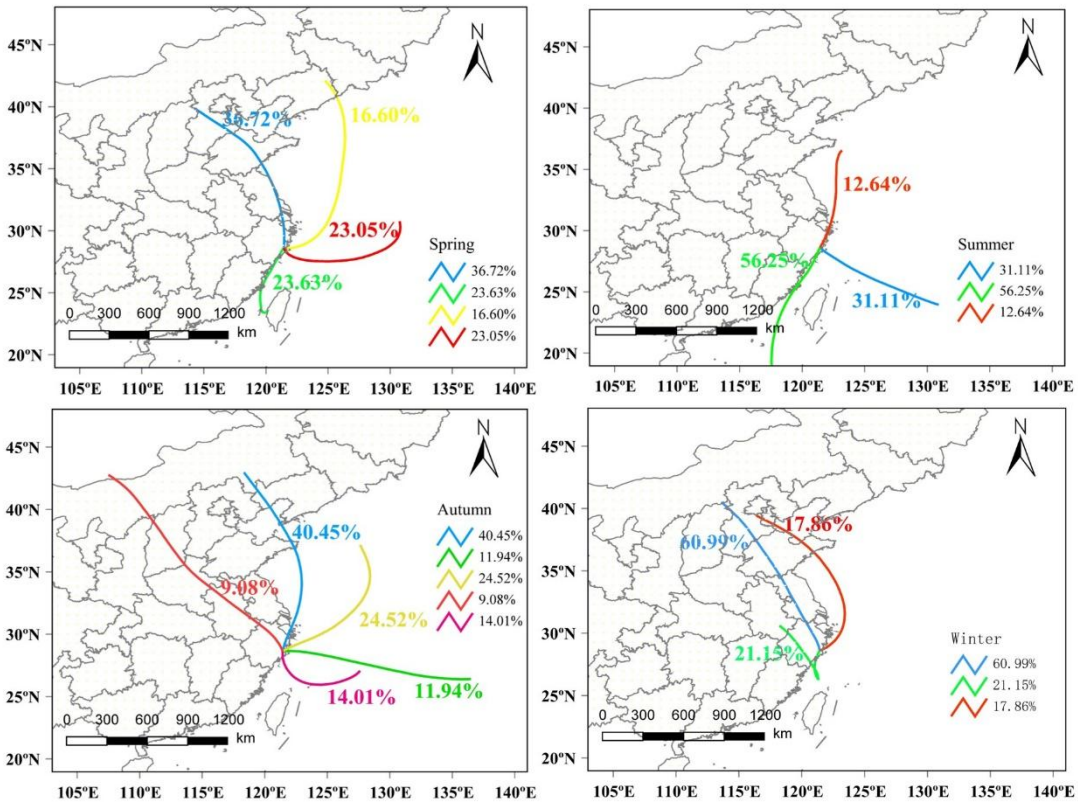



**Fig. 9** Seasonal clusters of 72 h backward trajectories arriving at Hongjia

**Table 2** Seasonal trajectory clusters and associated $CO_2$ concentrations at Hongjia during the observation period

| Season | Cluster | All traj. n | All traj. % | Mean $CO_2$ ($\times10^{-6}$) | High-value trajectories | | Low-value trajectories | | Season mean ($\times10^{-6}$) |
|---|---|---|---|---|---|---|---|---|---|
| | | | | | n | % | n | % | |
| Spring | 1 | 188 | 36.72 | 445.7 | 39 | 7.65 | 12 | 2.35 | 442.9 |
| | 2 | 121 | 23.63 | 448.0 | 45 | 8.82 | 21 | 4.12 | |
| | 3 | 85 | 16.60 | 438.4 | 3 | 0.59 | 19 | 3.73 | |
| | 4 | 118 | 23.05 | 436.7 | 15 | 2.94 | 50 | 9.80 | |
| Summer | 1 | 229 | 31.11 | 430.4 | 19 | 2.88 | 80 | 12.14 | 437.4 |
| | 2 | 414 | 56.25 | 441.1 | 97 | 14.72 | 41 | 6.22 | |
| | 3 | 93 | 12.64 | 438.4 | 16 | 2.43 | 11 | 1.67 | |
| Autumn | 1 | 254 | 40.45 | 436.9 | 45 | 7.28 | 36 | 5.83 | 436.3 |
| | 2 | 75 | 11.94 | 430.6 | 6 | 0.97 | 30 | 4.85 | |
| | 3 | 154 | 24.52 | 435.6 | 31 | 5.02 | 34 | 5.50 | |
| | 4 | 57 | 9.08 | 444.0 | 23 | 3.72 | 2 | 0.32 | |
| | 5 | 88 | 14.01 | 435.3 | 19 | 3.07 | 22 | 3.56 | |
| Winter | 1 | 222 | 60.99 | 450.2 | 46 | 12.67 | 38 | 10.47 | 449.5 |
| | 2 | 77 | 21.15 | 449.3 | 20 | 5.51 | 23 | 6.34 | |
| | 3 | 65 | 17.86 | 447.7 | 7 | 1.93 | 12 | 3.31 | |

$CO_2$ means are in $\times10^{-6}$. Trajectory counts and frequencies include all trajectories, whereas concentration means and high/low counts use valid concentration-matched trajectories. High and low percentages use the seasonal valid sample sizes as denominators: 510, 659, 618, and 363 in spring, summer, autumn, and winter, respectively. Seasonal means in this table refer to trajectories at 6 h intervals and differ from the hourly observation samples used elsewhere.

## Seasonal distribution of potential $CO_2$ source regions

Figure 10 shows the seasonal distributions of WPSCF at Hongjia. Higher WPSCF values indicate a greater probability of association with high $CO_2$ concentrations at the station (Ashbaugh et al., 1985; Lupu & Maenhaut, 2002). In spring, high values were concentrated in Fujian and Guangdong, consistent with the influence of cluster 2. Western Zhejiang also showed relatively high potential source influence, which may reflect terrain and anthropogenic emissions. In summer, high values were widely distributed across central and western Zhejiang and much of Fujian. Their spatial distribution closely followed cluster 2, the dominant summer pathway, indicating the influence of air transported from the South China Sea along the Zhejiang–Fujian coast.

Autumn had the broadest distribution of potential source regions, with high WPSCF values mainly over Anhui, Jiangsu, and Zhejiang and the highest values (> 0.8) near the Shandong–Anhui border. Increased energy use and industrial activity in upstream regions during the transition to the heating season may contribute to these features, while northern air associated with cluster 4 may carry additional $CO_2$. In winter, the high-value area was smaller than in autumn, with centers mainly over central and eastern Anhui and southwestern Zhejiang. Together with the trajectory clusters, particularly autumn cluster 4 and winter cluster 1, the potential source patterns point upstream toward high-emission regions such as Shanxi and Henan. These associations indicate persistent continental transport influences from North China during autumn and winter, consistent with transport-related $CO_2$ variability reported in eastern China (Fu et al., 2026; Liu et al., 2018).

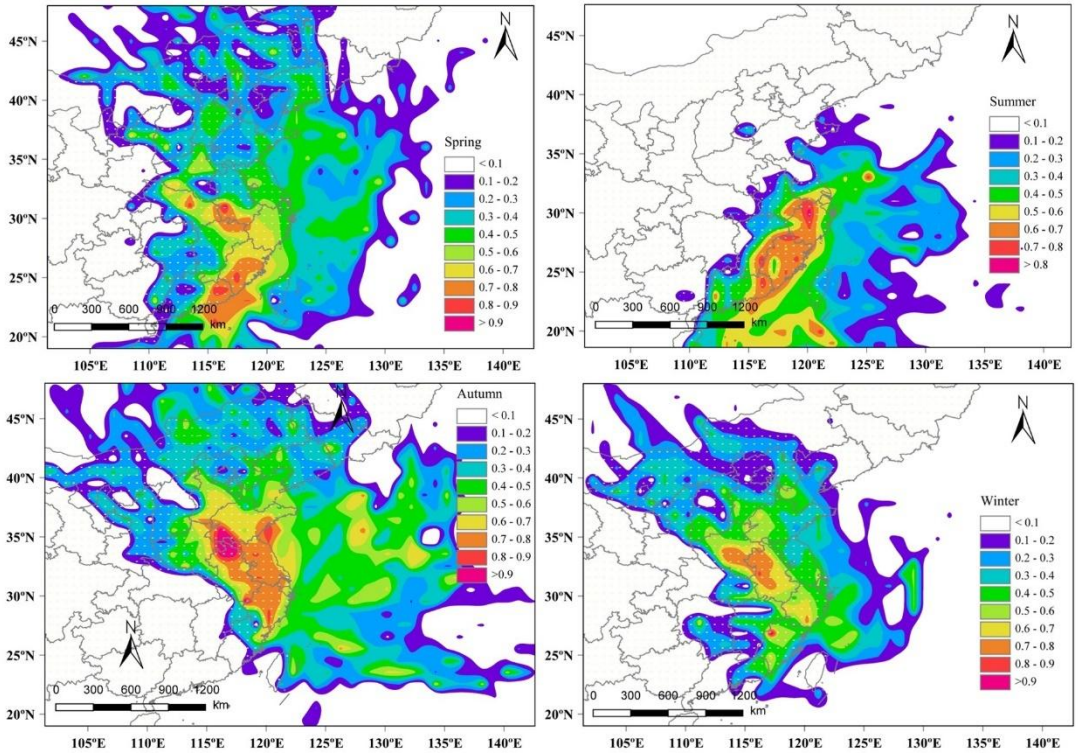



**Fig. 10** Seasonal distributions of the weighted potential source contribution function (WPSCF) for $CO_2$ at Hongjia

Characteristic concentrations based on over-ocean fraction and local winds

To describe the marine versus terrestrial portions of each pathway continuously, the 73 hourly endpoints of each 72 h trajectory, including the arrival endpoint, were classified using the land–sea mask. The over-ocean fraction f was defined as the proportion of endpoints located over the ocean. Trajectories were classified consistently as continental for $f \leq 0.2$, mixed for $0.2 < f < 0.8$, and marine for $f \geq 0.8$. These criteria were applied in Figs. 11 and 12 and Table 3. The categories

contained 333, 897, and 920 valid concentration-matched trajectories, respectively. This classification describes the proportion of a pathway over land or sea and does not directly quantify marine or continental contributions to $CO_2$.

For illustration, the mean over-ocean fractions of summer cluster 1 and autumn cluster 2 were 0.92 and 0.97, respectively, whereas those of autumn cluster 4 and winter cluster 1 were 0.06 and 0.15. Summer cluster 2 and spring cluster 3 had mean fractions of 0.71 and 0.76, indicating coastal or mixed pathways. These cluster means describe pathway characteristics; each trajectory was nevertheless classified using its own f value. In Fig. 11a, the mean concentrations in the five over-ocean fraction bins were 449.2, 444.9, 442.0, 440.9, and 435.3 × $10^{-6}$, respectively, showing a decreasing trend. The continental and marine groups had means of 449.2 × $10^{-6}$ and 435.3 × $10^{-6}$, a difference of 13.9 × $10^{-6}$. Across all 2,150 valid trajectories, the Pearson correlation between f and $CO_2$ at arrival was −0.367, indicating that trajectories with a larger marine fraction generally corresponded to lower concentrations. The direction of this association is consistent with observations distinguishing maritime and continental air at other coastal stations (Brunke et al., 2004; Derwent et al., 2002).

Additional local wind filters were applied to the marine group to identify low-concentration observations with stronger marine influence (Fig. 11b). The mean for $f \geq 0.8$ was 435.3 × $10^{-6}$ (n = 920). It decreased to 431.5 × $10^{-6}$ when restricted to SE–S winds (n = 247) and to 425.8 × $10^{-6}$ when the additional wind-speed criterion of ≥ 3 m $s^{-1}$ was applied (n = 63). Without restricting the trajectory pathway, the same marine-sector and wind-speed filters yielded a mean of 427.4 × $10^{-6}$ (n = 86). The SE–S sector was defined as $123.75° \leq \theta < 191.25°$, and the W–WSW sector as $236.25° \leq \theta < 281.25°$. Weak westerlies were defined as W–WSW winds with 0.3 ≤ wind speed < 1.5 m $s^{-1}$. Confidence intervals shown in Fig. 11 were obtained from 3,000 bootstrap replicates using UTC days as blocks; bootstrap resampling provides an estimate of sampling uncertainty (Efron & Tibshirani, 1993).

The value of 425.8 × $10^{-6}$ is a mean under specific screening criteria and provides a low-concentration reference for combined marine-pathway and stronger marine-sector winds. It should not be treated as a constant annual marine background. Of these 63 observations, 47 occurred in summer and 57 between April and September, whereas only three occurred in winter. Their representativeness is therefore mainly restricted to the warm season. This interpretation is consistent with the dependence of background estimates on filtering criteria (Fang et al., 2015; Ruckstuhl et al., 2012).

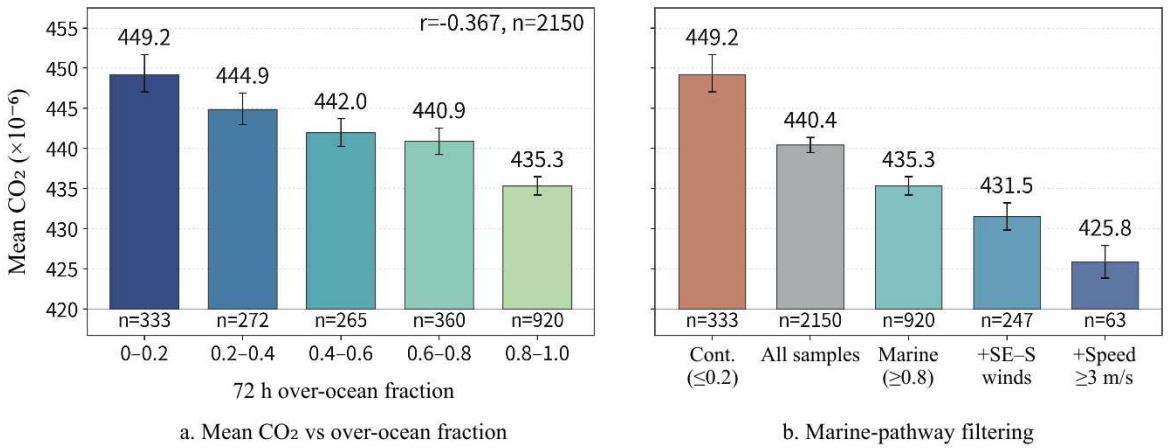



**Fig. 11** $CO_2$ concentrations by trajectory over-ocean fraction and local wind conditions. (a) Mean $CO_2$ versus the over-ocean fraction of 72 h trajectories. (b) Stepwise screening of marine-pathway concentrations. Continental (Cont.) pathways and all samples are reference groups; the last three groups apply $f \geq 0.8$, followed by the additional SE–S wind criterion and then speed $\geq 3$ m s$^{-1}$. n is the valid sample size; error bars are 95% confidence intervals from 3,000 bootstrap replicates using UTC days as blocks

To examine the combined associations with trajectory pathways and local winds, 2,010 trajectories with valid $CO_2$ and wind observations were cross-tabulated (Fig. 12). The same continental, mixed, and marine categories were used. Local winds were divided into three groups: SE–S winds with speeds $\geq 3$ m s$^{-1}$; other valid wind conditions; and W–WSW winds with $0.3 \leq$ speed $< 1.5$ m s$^{-1}$. "Other valid wind conditions" included observations that met neither of the two specific wind criteria and were not assumed to represent a background free of local emission influence.

Within the other-wind group, mean $CO_2$ increased from $435.1 \times 10^{-6}$ for marine pathways (n = 770) to $441.5 \times 10^{-6}$ for mixed pathways (n = 776) and $448.1 \times 10^{-6}$ for continental pathways (n = 291). The difference between the marine and continental means was $13.0 \times 10^{-6}$. Within every pathway category, weak-westerly means were higher than those under other valid wind conditions: by $11.7 \times 10^{-6}$ for marine pathways, $12.8 \times 10^{-6}$ for mixed pathways, and $6.9 \times 10^{-6}$ for continental pathways. The corresponding weak-westerly means were 446.8, 454.4, and 455.0 $\times 10^{-6}$. The lowest mean, $425.8 \times 10^{-6}$ (n = 63), occurred for marine pathways combined with stronger SE–S winds. The highest, $455.0 \times 10^{-6}$, occurred for continental pathways combined with weak westerlies, but this group contained only 16 observations and is interpreted descriptively. There were no valid observations for continental pathways combined with stronger SE–S winds, preventing a marine–continental comparison under that wind condition. Differences among wind groups varied by pathway category, so regional transport and local influences cannot be treated as fixed, independent, additive contributions.

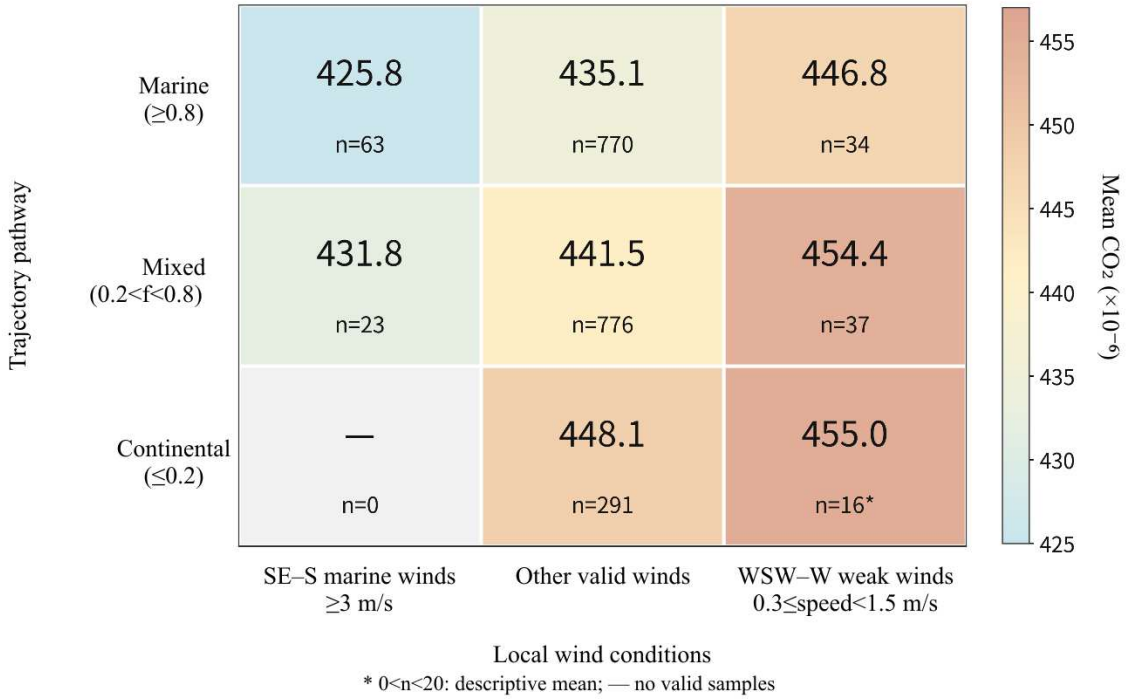



**Fig. 12** Mean $CO_2$ concentrations at Hongjia by trajectory pathway and local wind condition. Rows represent marine ($f \geq 0.8$), mixed ($0.2 < f < 0.8$), and continental ($f \leq 0.2$) pathways. Columns represent SE–S winds with speed ≥ 3 m $s^{-1}$, other valid wind conditions, and W–WSW winds with $0.3 \leq$ speed < 1.5 m $s^{-1}$. Cells show the mean concentration ($\times 10^{-6}$) and n. A dash indicates no valid observations; an asterisk indicates $0 < n < 20$, for which the mean is descriptive only

**Table 3** Characteristic $CO_2$ concentrations at Hongjia under different screening criteria

| Characteristic level | Trajectory and local wind criteria | $CO_2$ ($\times 10^{-6}$) | Statistical interpretation |
|---|---|---|---|
| Marine-pathway low-concentration reference | $f \geq 0.8$; SE–S winds with speed ≥ 3 m $s^{-1}$ | 425.8 | Conditional mean (n = 63), mainly representative of the warm season |
| Continental-pathway characteristic level | $f \leq 0.2$; no additional wind criterion, or other valid wind conditions | 448.1–449.2 | Range of means under two filters (n = 291 and 333, respectively); not a confidence interval |
| Weak-westerly high-concentration level | All f; W–WSW winds with $0.3 \leq$ speed < 1.5 m $s^{-1}$ | 451.5 (winter 459.3) | Mean across the observation period (n = 87); winter subset mean (n = 24) |

Table 3 summarizes the characteristic concentrations under different screening criteria. Marine pathways combined with stronger marine-sector winds had a mean of $425.8 \times 10^{-6}$. Continental pathways without additional wind filtering had a mean of $449.2 \times 10^{-6}$ (n = 333), while continental pathways restricted to other valid wind conditions had a mean of $448.1 \times 10^{-6}$ (n = 291). The interval of $448.1–449.2 \times 10^{-6}$ therefore represents means under two screening conditions and is not a confidence interval. Weak westerlies across all pathway categories had a mean of $451.5 \times 10^{-6}$ (n = 87), increasing to $459.3 \times 10^{-6}$ in winter (n = 24).

These values describe different conditional samples rather than independent source endmembers. Cross-tabulation indicates that land–sea pathway differences, local transport, and dispersion jointly influence $CO_2$ at Hongjia. Diurnal and seasonal photosynthetic and respiratory exchange can also modify air masses from each pathway category, as discussed above. The statistics constrain concentration levels under different conditions but do not independently quantify local anthropogenic emissions or oceanic uptake. Such separation requires additional constraints, including emission inventories, boundary layer observations, atmospheric transport footprints, or flux measurements (Lauvaux et al., 2016; Lin et al., 2003; Turnbull et al., 2015).

## Conclusions

Atmospheric $CO_2$ observations at Hongjia from April 2023 to November 2024 were used to characterize temporal variability and its associations with meteorological conditions, regional transport, and land–sea pathways. The main findings are as follows.

**1.** $CO_2$ exhibited pronounced seasonal and diurnal variability. The mean concentration was $(440.61 \pm 14.0) \times 10^{-6}$, lower than at inland Lin'an and consistent with dilution by marine air at the coastal station. Concentrations were highest in winter and lowest in summer and autumn, with a monthly maximum in January and minimum in July. The seasonal amplitude was larger than at Lin'an. The diurnal cycle had a single afternoon minimum, with higher concentrations around dawn, reflecting the combined effects of photosynthesis, respiration, and boundary layer variability.

**2.** Meteorological conditions were important correlates of $CO_2$ variability. Wind speed had the strongest overall negative association in every season, with higher concentrations under weak winds and declining concentrations as wind speed increased. This pattern is consistent with accumulation from local and nearby sources under inhibited dispersion. The negative temperature correlation was strongest in autumn, while relative humidity was positively correlated with $CO_2$. W–WSW winds corresponded to the highest concentrations in all seasons, consistent with nearby industrial sources and weak ventilation. Easterly flow may transport emissions from the eastern industrial area in winter, whereas southerly marine flow was associated with lower concentrations.

**3.** Cross-tabulation of trajectories and local winds demonstrated associations with both regional pathways and local wind conditions. Using the common criteria of continental ($f \leq 0.2$), mixed ($0.2 < f < 0.8$), and marine ($f \geq 0.8$) pathways, f was negatively correlated with $CO_2$ ($r = -0.367$).

Marine pathways combined with SE–S winds and speeds ≥ 3 m $s^{-1}$ had a mean of 425.8 × $10^{-6}$ (n = 63), providing a marine-influenced low-concentration reference mainly for the warm season. Continental-pathway means ranged from 448.1 to 449.2 × $10^{-6}$ under different local wind filters. Weak westerlies across pathways had a mean of 451.5 × $10^{-6}$, increasing to 459.3 × $10^{-6}$ in winter. Within pathway categories, weak-westerly means exceeded those under other valid wind conditions by 6.9–12.8 × $10^{-6}$. These differences also depend on seasonal sample composition and dispersion and cannot be interpreted as independent local anthropogenic increments. WPSCF indicated potential source regions along the Zhejiang–Fujian coast, near the Jiangsu–Anhui border, and in North China, with autumn and winter pathways extending upstream toward high-emission regions such as Shanxi and Henan.

**4.** $CO_2$ variability at Hongjia reflects the combined influence of regional transport, local emissions and dispersion, and terrestrial ecosystem exchange at the coastal land–sea interface. Lower summer and autumn concentrations were associated with marine pathways, southerly winds, and active vegetation growth. Higher winter concentrations were associated with reduced vegetation uptake, weaker dispersion, and continental transport. Elevated concentrations under weak westerlies were consistent with nearby emission accumulation, while marine pathways combined with stronger marine-sector winds corresponded to lower concentrations. These conditional means provide concentration references for different transport and wind regimes. Further separation of source–sink contributions requires emission inventories, boundary layer observations, or flux measurements.

## Statements and declarations

**Funding:** This research was supported by the Joint Funds of the Zhejiang Provincial Natural Science Foundation of China under Grant No. LZJMZ23D050002.

**Competing interests:** The authors have no relevant financial or non-financial interests to disclose.

**Author contributions:** Qiao Lu developed the research concept and defined the study objectives. Huihong Xu established the analytical framework and designed the methodological approach. Meng Shan, Weidong Dai and Wenzhi Zhang coordinated the station observations and collected the $CO_2$ and meteorological data. Qiao Lu and Ziqi Zhang performed data quality control, preprocessing, and dataset organization. Qiao Lu and Kai Wang conducted the statistical analyses and comparisons of temporal variability and meteorological influences. Qiao Lu and Zhimei Weng performed the backward-trajectory clustering and potential source contribution analyses.

Qiao Lu wrote the first draft of the manuscript. Huihong Xu revised the overall structure, logical flow, and organization of the manuscript. All authors reviewed and approved the final version of the manuscript.

**Data availability:** The observational data used in this study are subject to institutional access restrictions and are therefore not publicly available. Requests for access may be directed to the corresponding author and will be considered subject to approval by the relevant data provider and applicable conditions of use.

**Ethical responsibilities:** All authors have read, understood, and have complied as applicable with the statement on "Ethical responsibilities of Authors" as found in the Instructions for Authors.

## References


Ashbaugh, L. L., Malm, W. C., & Sadeh, W. Z. (1985). A residence time probability analysis of sulfur concentrations at Grand Canyon National Park. *Atmospheric Environment*, *19*(8), 1263–1270. https://doi.org/10.1016/0004-6981(85)90256-2

Baer, D. S., Paul, J. B., Gupta, M., & O'Keefe, A. (2002). Sensitive absorption measurements in the near-infrared region using off-axis integrated-cavity-output spectroscopy. *Applied Physics B*, *75*(2-3), 261–265. https://doi.org/10.1007/s00340-002-0971-z

Baldocchi, D. D. (2003). Assessing the eddy covariance technique for evaluating carbon dioxide exchange rates of ecosystems: past, present and future. *Global Change Biology*, *9*(4), 479–492. https://doi.org/10.1046/j.1365-2486.2003.00629.x

Ballantyne, A. P., Alden, C. B., Miller, J. B., Tans, P. P., & White, J. W. C. (2012). Increase in observed net carbon dioxide uptake by land and oceans during the past 50 years. *Nature*, *488*(7409), 70–72. https://doi.org/10.1038/nature11299

Brunke, E.-G., Labuschagne, C., Parker, B., Scheel, H. E., & Whittlestone, S. (2004). Baseline air mass selection at Cape Point, South Africa: application of 222Rn and other filter criteria to $CO_2$. *Atmospheric Environment*, *38*(33), 5693–5702. https://doi.org/10.1016/j.atmosenv.2004.04.024

Chen, C.-T. A., Huang, T.-H., Chen, Y.-C., Bai, Y., He, X., & Kang, Y. (2013). Air–sea exchanges of $CO_2$ in the world's coastal seas. *Biogeosciences*, *10*(10), 6509–6544. https://doi.org/10.5194/bg-10-6509-2013

Cheng, S., An, X., Zhou, L., Tans, P. P., & Jacobson, A. (2017). Atmospheric $CO_2$ at Waliguan station in China: Transport climatology, temporal patterns and source-sink region representativeness. *Atmospheric Environment*, *159*, 107–116. https://doi.org/10.1016/j.atmosenv.2017.03.055

Cheng, S., Zhou, L., Tans, P. P., An, X., & Liu, Y. (2018). Comparison of atmospheric $CO_2$ mole fractions and source–sink characteristics at four WMO/GAW stations in China. *Atmospheric Environment*, *180*, 216–225. https://doi.org/10.1016/j.atmosenv.2018.03.010

Derwent, R. G., Ryall, D. B., Manning, A. J., Simmonds, P. G., O'Doherty, S., Biraud, S., Ciais, P., Ramonet, M., & Jennings, S. G. (2002). Continuous observations of carbon dioxide at Mace Head, Ireland from 1995 to 1999 and its net European ecosystem exchange. *Atmospheric Environment*, *36*(17), 2799–2807. https://doi.org/10.1016/s1352-2310(02)00203-0

Draxler, R. R., & Hess, G. D. (1998). An overview of the HYSPLIT_4 modelling system for trajectories, dispersion and deposition. *Australian Meteorological Magazine*, *47*(4), 295–308. https://doi.org/10.1071/es98032

Duan, Z., Yang, Y., Wang, L., Liu, C., Fan, S., Chen, C., Tong, Y., Lin, X., & Gao, Z. (2021). Temporal characteristics of carbon dioxide and ozone over a rural-cropland area in the Yangtze River Delta of eastern China. *Science of The Total Environment*, *757*, Article 143750. https://doi.org/10.1016/j.scitotenv.2020.143750

Efron, B., & Tibshirani, R. J. (1993). *An introduction to the bootstrap*. Chapman & Hall. https://doi.org/10.1007/978-1-4899-4541-9

Fang, S. X., Tans, P. P., Steinbacher, M., Zhou, L. X., & Luan, T. (2015). Comparison of the regional $CO_2$ mole fraction filtering approaches at a WMO/GAW regional station in China. *Atmospheric Measurement Techniques*, *8*(12), 5301–5313. https://doi.org/10.5194/amt-8-5301-2015

Fang, S. X., Zhou, L. X., Tans, P. P., Ciais, P., Steinbacher, M., Xu, L., & Luan, T. (2014). In situ measurement of atmospheric $CO_2$ at the four WMO/GAW stations in China. *Atmospheric Chemistry and Physics*, *14*(5), 2541–2554. https://doi.org/10.5194/acp-14-2541-2014

Friedlingstein, P., O'Sullivan, M., Jones, M. W., Andrew, R. M., Bakker, D. C. E., Hauck, J., Landschützer, P., Le Quéré, C., Luijkx, I. T., Peters, G. P., Peters, W., Pongratz, J., Schwingshackl, C., Sitch, S., Canadell, J. G., Ciais, P., Jackson, R. B., Alin, S. R., Anthoni, P., … Zheng, B. (2023). Global Carbon Budget 2023. *Earth System Science Data*, *15*(12), 5301–5369. https://doi.org/10.5194/essd-15-5301-2023

Fu, S., Qing, X., Zang, K., Lin, Y., Liu, S., Chen, Y., Chen, B., Gao, W., Steinbacher, M., & Fang, S. (2026). Observational insights into atmospheric $CO_2$ and CO at the urban canopy layer top in Metropolitan Shanghai, China. *Atmospheric Chemistry and Physics*, *26*(8), 5477–5496. https://doi.org/10.5194/acp-26-5477-2026

Graven, H. D., Keeling, R. F., Piper, S. C., Patra, P. K., Stephens, B. B., Wofsy, S. C., Welp, L. R., Sweeney, C., Tans, P. P., Kelley, J. J., Daube, B. C., Kort, E. A., Santoni, G. W., & Bent, J. D. (2013). Enhanced seasonal exchange of $CO_2$ by northern ecosystems since 1960. *Science*, *341*(6150), 1085–1089. https://doi.org/10.1126/science.1239207

Intergovernmental Panel on Climate Change (2021). *Climate change 2021: The physical science basis. Contribution of Working Group I to the Sixth Assessment Report of the Intergovernmental Panel on Climate Change*. Cambridge University Press. https://doi.org/10.1017/9781009157896

Lauvaux, T., Miles, N. L., Deng, A., Richardson, S. J., Cambaliza, M. O., Davis, K. J., Gaudet, B., Gurney, K. R., Huang, J., O'Keefe, D., Song, Y., Karion, A., Oda, T., Patarasuk, R., Razlivanov, I., Sarmiento, D., Shepson, P., Sweeney, C., Turnbull, J., & Wu, K. (2016). High-resolution atmospheric

inversion of urban $CO_2$ emissions during the dormant season of the Indianapolis Flux Experiment (INFLUX). *Journal of Geophysical Research: Atmospheres*, *121*(10), 5213–5236. https://doi.org/10.1002/2015jd024473

Lin, J. C., Gerbig, C., Wofsy, S. C., Andrews, A. E., Daube, B. C., Davis, K. J., & Grainger, C. A. (2003). A near-field tool for simulating the upstream influence of atmospheric observations: The Stochastic Time-Inverted Lagrangian Transport (STILT) model. *Journal of Geophysical Research: Atmospheres*, *108*(D16), Article 4244. https://doi.org/10.1029/2002jd003161

Liu, L., Tans, P. P., Xia, L., Zhou, L., & Zhang, F. (2018). Analysis of patterns in the concentrations of atmospheric greenhouse gases measured in two typical urban clusters in China. *Atmospheric Environment*, *173*, 343–354. https://doi.org/10.1016/j.atmosenv.2017.11.023

Lupu, A., & Maenhaut, W. (2002). Application and comparison of two statistical trajectory techniques for identification of source regions of atmospheric aerosol species. *Atmospheric Environment*, *36*(36-37), 5607–5618. https://doi.org/10.1016/s1352-2310(02)00697-0

Natural Earth (n.d.). *Land polygons at 1:10 million scale*. https://www.naturalearthdata.com/downloads/10m-physical-vectors/10m-land/

Nisbet, E., & Weiss, R. (2010). Top-down versus bottom-up. *Science*, *328*(5983), 1241–1243. https://doi.org/10.1126/science.1189936

Pataki, D. E., Alig, R. J., Fung, A. S., Golubiewski, N. E., Kennedy, C. A., McPherson, E. G., Nowak, D. J., Pouyat, R. V., & Romero Lankao, P. (2006). Urban ecosystems and the North American carbon cycle. *Global Change Biology*, *12*(11), 2092–2102. https://doi.org/10.1111/j.1365-2486.2006.01242.x

Peters, W., Jacobson, A. R., Sweeney, C., Andrews, A. E., Conway, T. J., Masarie, K., Miller, J. B., Bruhwiler, L. M. P., Pétron, G., Hirsch, A. I., Worthy, D. E. J., van der Werf, G. R., Randerson, J. T., Wennberg, P. O., Krol, M. C., & Tans, P. P. (2007). An atmospheric perspective on North American carbon dioxide exchange: CarbonTracker. *Proceedings of the National Academy of Sciences*, *104*(48), 18925–18930. https://doi.org/10.1073/pnas.0708986104

Ruckstuhl, A. F., Henne, S., Reimann, S., Steinbacher, M., Vollmer, M. K., O'Doherty, S., Buchmann, B., & Hueglin, C. (2012). Robust extraction of baseline signal of atmospheric trace species using local regression. *Atmospheric Measurement Techniques*, *5*(11), 2613–2624. https://doi.org/10.5194/amt-5-2613-2012

Stein, A. F., Draxler, R. R., Rolph, G. D., Stunder, B. J. B., Cohen, M. D., & Ngan, F. (2015). NOAA's HYSPLIT atmospheric transport and dispersion modeling system. *Bulletin of the American Meteorological Society*, *96*(12), 2059–2077. https://doi.org/10.1175/bams-d-14-00110.1

Stohl, A. (1998). Computation, accuracy and applications of trajectories—A review and bibliography. *Atmospheric Environment*, *32*(6), 947–966. https://doi.org/10.1016/s1352-2310(97)00457-3

Stull, R. B. (1988). *An introduction to boundary layer meteorology*. Kluwer Academic Publishers. https://doi.org/10.1007/978-94-009-3027-8

Turnbull, J. C., Sweeney, C., Karion, A., Newberger, T., Lehman, S. J., Tans, P. P., Davis, K. J., Lauvaux, T., Miles, N. L., Richardson, S. J., Cambaliza, M. O., Shepson, P. B., Gurney, K., Patarasuk, R., & Razlivanov, I. (2015). Toward quantification and source sector identification of fossil fuel $CO_2$

emissions from an urban area: Results from the INFLUX experiment. *Journal of Geophysical Research: Atmospheres*, *120*(1), 292–312. https://doi.org/10.1002/2014jd022555

Wang, Y. Q. (2014). MeteoInfo: GIS software for meteorological data visualization and analysis. *Meteorological Applications*, *21*(2), 360–368. https://doi.org/10.1002/met.1345

Wanninkhof, R., Park, G.-H., Takahashi, T., Sweeney, C., Feely, R., Nojiri, Y., Gruber, N., Doney, S. C., McKinley, G. A., Lenton, A., Le Quéré, C., Heinze, C., Schwinger, J., Graven, H., & Khatiwala, S. (2013). Global ocean carbon uptake: magnitude, variability and trends. *Biogeosciences*, *10*(3), 1983–2000. https://doi.org/10.5194/bg-10-1983-2013

Wei, C., Wang, M., Fu, Q., Dai, C., Huang, R., & Bao, Q. (2020). Temporal characteristics of greenhouse gases ($CO_2$ and $CH_4$) in the megacity Shanghai, China: Association with air pollutants and meteorological conditions. *Atmospheric Research*, *235*, Article 104759. https://doi.org/10.1016/j.atmosres.2019.104759

World Meteorological Organization (2024). *WMO Greenhouse Gas Bulletin No. 20*. https://wmo.int/resources/publication-series/greenhouse-gas-bulletin/wmo-greenhouse-gas-bulletin-no-20